

# EFFECT OF BEAM CHROMATICITY ON FOREGROUNDS IN WIDE-FIELD MEASUREMENTS OF REDSHIFTED 21 CM POWER SPECTRA

NITHYANANDAN THYAGARAJAN<sup>1\*</sup>, TBD

*Draft version January 13, 2016*

## ABSTRACT

*Keywords:* cosmology: observations — dark ages, reionization, first stars — large-scale structure of universe — methods: statistical — radio continuum: galaxies — techniques: interferometric

### 1. INTRODUCTION

The period in the history of the Universe characterized by the transition of neutral hydrogen in the intergalactic medium (IGM) to a fully ionized state due to the formation of radiating objects such as the first stars and galaxies is referred to as the Epoch of Reionization (EoR). This is an important period of nonlinear growth of matter density perturbations and astrophysical evolution leading to the large scale structure observed currently in the Universe. And yet, this period in the Universe’s history has remained poorly probed to date with observations.

The redshifted neutral hydrogen from the IGM in this epoch has been identified to be one of the most promising and direct probes of the EoR (Sunyaev & Zeldovich 1972; Scott & Rees 1990; Madau et al. 1997; Tozzi et al. 2000; Iliev et al. 2002). Numerous experiments using low frequency radio telescopes targeting the redshifted 21 cm line from the spin-flip transition of HI have become operational such as the Murchison Widefield Array (MWA; Lonsdale et al. 2009; Bowman et al. 2013; Tingay et al. 2013), the Precision Array for Probing the Epoch of Reionization (PAPER; Parsons et al. 2010), the Low Frequency Array (LOFAR; van Haarlem et al. 2013) and the Giant Metrewave Radio Telescope EoR experiment (GMRT; Paciga et al. 2013). These instruments have sufficient sensitivity for a statistical detection of the EoR signal via estimating the spatial power spectrum of the redshifted HI temperature fluctuations (Beardsley et al. 2013; Thyagarajan et al. 2013). These instruments are intended to be precursors and pathfinders to the next generation of low frequency radio observatories such as the Hydrogen Epoch of Reionization Array<sup>3</sup> (HERA; DeBoer et al. 2015) and the Square Kilometre Array<sup>4</sup> (SKA). These next-generation instruments will advance the capability from a mere statistical detection of the signal to a direct three-dimensional tomographic imaging of the HI during the EoR.

The most significant challenge to low frequency EoR observations arises from the extremely bright Galactic and extragalactic foreground synchrotron emission which are  $\sim 10^4$  times stronger than the desired EoR signal (Di Matteo et al. 2002; Ali et al. 2008; Bernardi et al. 2009, 2010; Ghosh et al. 2012). All the current and future

instruments rely on the inherent differences in spatial isotropy and spectral smoothness between the EoR signal and the foregrounds to extract the EoR power spectrum (see, e.g., Furlanetto & Briggs 2004; Morales & Hewitt 2004; Zaldarriaga et al. 2004; Santos et al. 2005; Furlanetto et al. 2006; McQuinn et al. 2006; Morales et al. 2006; Wang et al. 2006; Gleser et al. 2008).

When expressed in the coordinate system of power spectrum measurements described by the three-dimensional wavenumber ( $k$ ), the foreground emission is restricted to a wedge-shaped region commonly referred to as the *foreground wedge* (Bowman et al. 2009; Liu et al. 2009, 2014a,b; Datta et al. 2010; Liu & Tegmark 2011; Ghosh et al. 2012; Morales et al. 2012; Parsons et al. 2012; Trott et al. 2012; Vedantham et al. 2012; Dillon et al. 2013; Pober et al. 2013; Thyagarajan et al. 2013; Dillon et al. 2014) whereas the EoR signal has spherical symmetry due to its isotropy which appears elongated along line of sight  $k$  modes due to peculiar velocity effects when dominated by matter density perturbations during early stages of reionization. The extreme dynamic range required to subtract foregrounds precisely demands high precision modeling of foregrounds as observed by modern wide-field instruments (Thyagarajan et al. 2015b,a).

### 2. THE HYDROGEN EPOCH OF REIONIZATION ARRAY

DeBoer et al.(2016)

### 3. DELAY SPECTRUM

(Parsons et al. 2012)

#### 3.1. The Wide-Field “Pitchfork” Effect

(Thyagarajan et al. 2015b,a)

### 4. SIMULATIONS

We simulate wide-field visibilities for 19-element HERA from all-sky antenna power pattern and foreground models using the PRISim<sup>5</sup> software package. The simulations cover 24 hr of observation in *drift* mode consisting of 80 accumulations spanning 1080 s each. The total bandwidth is 100 MHz centered on 150 MHz consisting of 128 channels with 781.125 kHz frequency resolution each. Models of the antenna power pattern and foregrounds are described below.

#### 4.1. Antenna Power Pattern

(Neben et al. 2015)

<sup>1</sup> Arizona State University, School of Earth and Space Exploration, Tempe, AZ 85287, USA

\* e-mail: t\_nithyanandan@asu.edu

<sup>3</sup> <http://reionization.org/>

<sup>4</sup> <https://www.skatelescope.org/>

<sup>5</sup> The Precision Radio Interferometry Simulator (PRISim) is publicly available at <https://github.com/nithyanandan/PRISim>

#### 4.2. Foreground Model

Our all-sky foreground model is the same as the one in Thyagarajan et al. (2015b). It consists of diffuse emission (de Oliveira-Costa et al. 2008) and point sources. The latter is obtained from a combination of the NRAO VLA Sky Survey (NVSS; Condon et al. 1998) at 1.4 GHz and the Sydney University Molonglo Sky Survey (SUMSS; Bock et al. 1999; Mauch et al. 2003) at 843 MHz with a mean spectral index of -0.83. The diffuse sky model has an angular resolution of 13'.74.

### 5. CHROMATICITY OF POWER PATTERN

The equation for delay spectrum describes the mapping between sky location of a foreground object and delay. The chromatic nature (variation with frequency) of the antenna power pattern results in a convolution of the geometrical mapping with the delay response of spectral chromaticity of the power pattern. This can result in a significant spillover of foreground power beyond the horizon delay limits especially in the case of foregrounds near the horizon.

Fig. 1 demonstrates the beyond-the-horizon spillover even from a flat-spectrum point source at different off-axis angles. The three panels correspond to delay spectra from different positions of the point source – 0° (left), 45° (middle) and 89° (right) – from the zenith. The phase centers are located at the source positions and hence the delay spectra are centered on  $\tau = 0$  ns. The response of the simulated dish power pattern (dashed line) is compared with that from an *Airy* pattern resulting from a nominal uniformly illuminated circular disk (solid line). The gray vertical lines correspond to the horizon limits at  $\pm 48.7$  ns for a 14.6 m antenna spacing.

At 0° off-axis, the *Airy* pattern has no spectral variation and thus appears as a straight vertical line centered at  $\tau = 0$  ns whereas the simulated power pattern is found to exhibit some spectral variation giving rise to the wings on either side of  $\tau = 0$  ns. As off-axis angle increases to 45°, both the power patterns clearly exhibit chromaticity. They have similar magnitudes inside the horizon limits but the chromaticity of the simulated power pattern is  $\sim 100$  times higher than that of an *Airy* pattern outside the horizon limits. In contrast, at 89° off-axis, the two patterns have similar chromaticity in delay modes outside the horizon limits but the simulated power pattern has  $\sim 100$  times more power inside the horizon limits indicating that the overall amplitude of the pattern at this location is higher relative to the nominal *Airy* pattern.

It is important to note that in a generic scenario where visibilities are not phased to a specific foreground location, the chromaticity of the power pattern will imprint itself on location of the foreground objects in delay space and will give rise to significant spillover especially from foregrounds near the horizon.

We investigate the effects of spectral chromaticity of the power pattern in more detail below.

#### 5.1. Directional Chromaticity of Power Pattern

We generalize the analysis above by computing the delay power spectrum of the power pattern along its spectral axis in every direction in an effort to study its per-

formance as a function of angle on the sky.

$$A'(l, m, \tau) = \int A(l, m, f) e^{-j2\pi f\tau} df \quad (1)$$

We define the directional chromaticity of antenna power pattern as:

$$C(l, m) = \frac{\int_{|\tau| > 60 \text{ ns}} |A'|^2 d\tau}{\int_{|\tau| > 60 \text{ ns}} d\tau} \quad (2)$$

where, the limit  $|\tau| > 60$  ns was chosen to represent a region well beyond the horizon limits ( $\pm 48.7$  ns) for a 14.6 m antenna spacing. It thus measures the average power arising out of chromaticity in each delay mode beyond  $|\tau| > 60$  ns.

Fig. 2 shows the directional chromaticity,  $C(l, m)$ , of the power patterns of an *Airy* disk for reference (left) and a simulated disk (middle) on an orthographic projection onto direction cosines. Their color scale is shown at the top for reference. The chromaticity of the *Airy* pattern is symmetric and always below 500. On the other hand, a simulated disk exhibits higher levels of chromaticity in the range 100–50,000. The ratio of their chromaticities is shown on the right with corresponding color scale on its right. The simulated disk is more chromatic than the nominal *Airy* disk by a factor between 100 and up to 10000. However, chromaticity in regions near the horizon which map to the horizon limits in the delay spectrum and have the most significant impact on spillover into the *EoR window* in the simulated disk are higher than that of an *Airy* disk only by factors  $\lesssim 4$ . Thus the simulated disk for HERA achieves reasonable control on the chromaticity near the horizon despite the very high levels near the center.

Also shown are the tracks (black dots) of point sources brighter than 50 Jy in the LST range 0–12 hrs. The solid circle near the bottom denotes the south celestial pole. It is noted that there are a few bright point sources that spend a majority of time in this LST range near the northern and southern horizons which will contaminate the measured visibilities on north-south antenna spacings. Future simulations of the dish power pattern must take the bright foreground locations, especially near the horizon, into account.

#### 5.2. Effect on Delay Power Spectrum

Now we consider the effect of chromaticity of the power pattern on the delay power spectrum.

We simulate visibilities from our foreground model using three different models for the antenna power pattern – *Airy* pattern, simulated dish, and a pattern at 150 MHz of the simulated dish assumed to be achromatic over the entire band.

Fig. 3 shows the delay power spectra of foregrounds obtained with the aforementioned models for power pattern. In all these panels, power spectra obtained with achromatic, *Airy* disk and simulated disk are shown in black, red, and blue respectively. The vertical gray lines denote the horizon limits for a 14.6 m antenna spacing. The full band delay power spectra of the foregrounds measured on a 14.6 m antenna spacing oriented eastward is shown in the top left panel. A clear

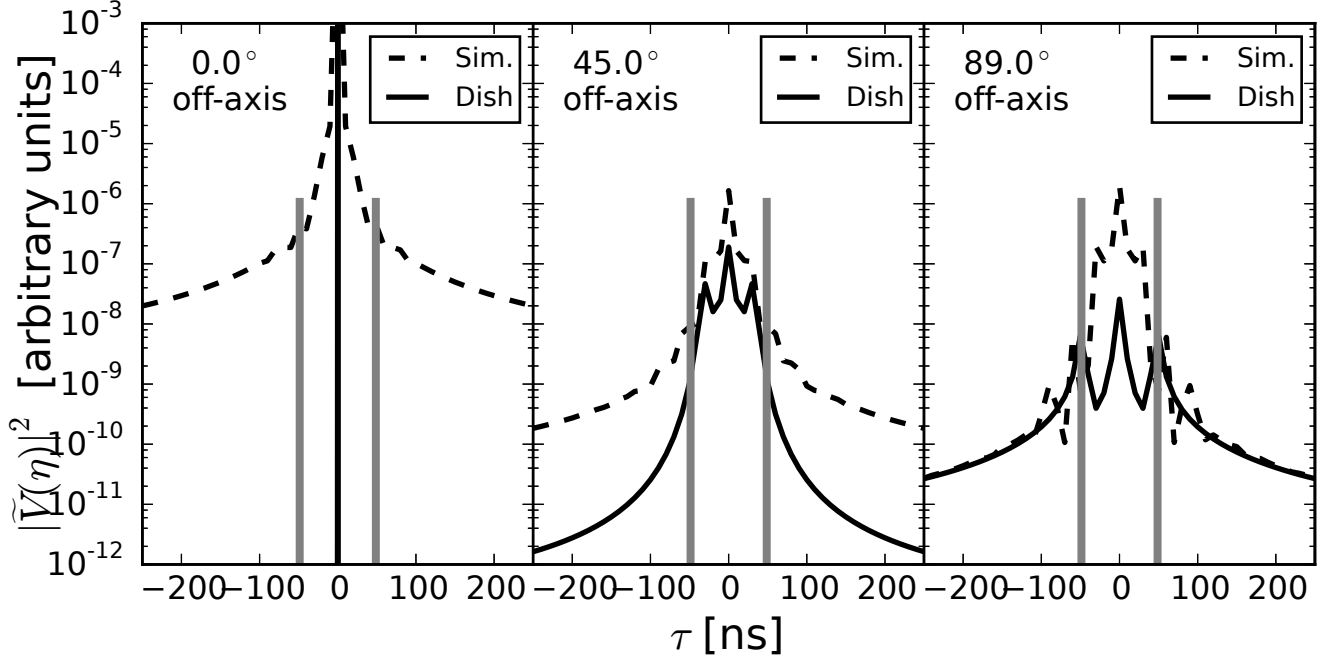


**Figure 1.** Chromaticity of antenna power pattern at directions off-axis.

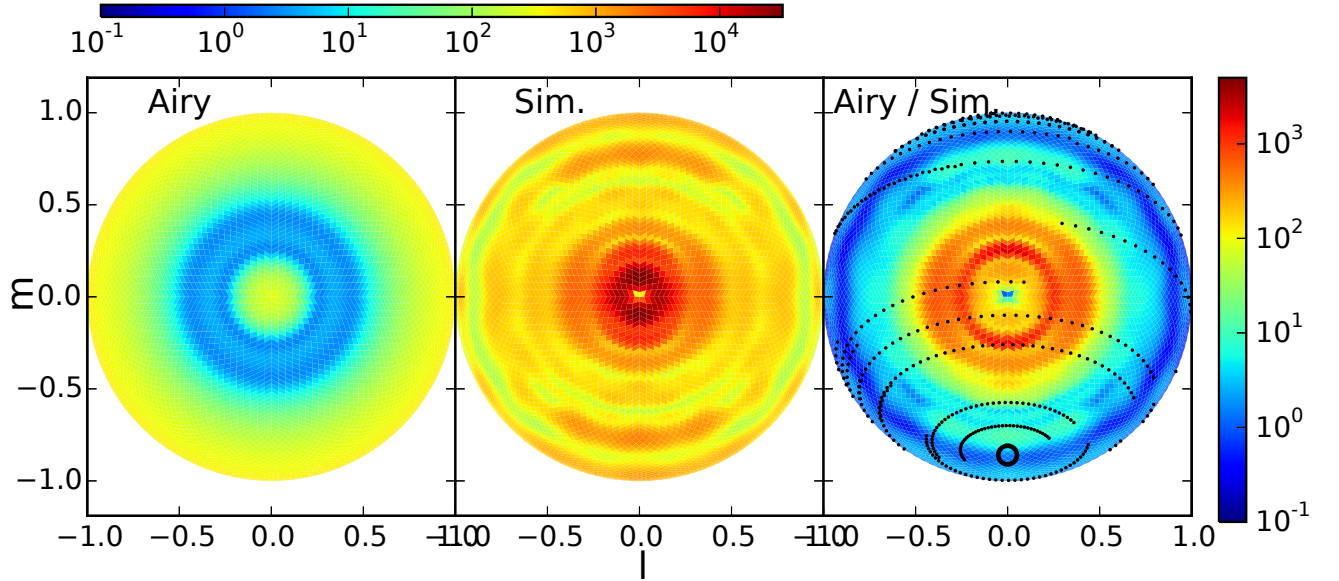


**Figure 2.** All-sky directional chromaticity of antenna power pattern.

trend of broadening of spillover-wings outside the horizon limits is seen with increasing chromaticity. For instance, the spillover from foreground delay power spectrum obtained with simulated dish pattern extends out to  $k_{\parallel} \approx \pm 0.14 h \text{ Mpc}^{-1}$ , with the *Airy* pattern it extends out to  $k_{\parallel} \approx \pm 0.08 h \text{ Mpc}^{-1}$ , while the achromatic beam extends it only out to  $k_{\parallel} \approx \pm 0.05 h \text{ Mpc}^{-1}$ . Thus an increase in chromaticity extends the foreground spillover into higher  $k_{\parallel}$ -modes making them inaccessible for EoR Hi signal detection.

Following the foreground removal strategy, the top middle panel shows these foreground delay spectra deconvolved using the complex delay CLEAN algorithm

(Taylor et al. 1999; Parsons & Backer 2009; Parsons et al. 2012). The CLEAN window covers delay bins between the horizon delay limits and extends further by three delay bins on each side of the horizon limit where a delay bin is of size inverse of the bandwidth. The panel at the top right shows the residuals left behind after deconvolution.

Owing to the chromaticity of power patterns, the spillover from foregrounds extends beyond the horizon limits, most severely in the simulated disk pattern. As a result the residuals have significant power remaining on either side of the horizon limits since the window for deconvolution is narrower than the extent of spillover along

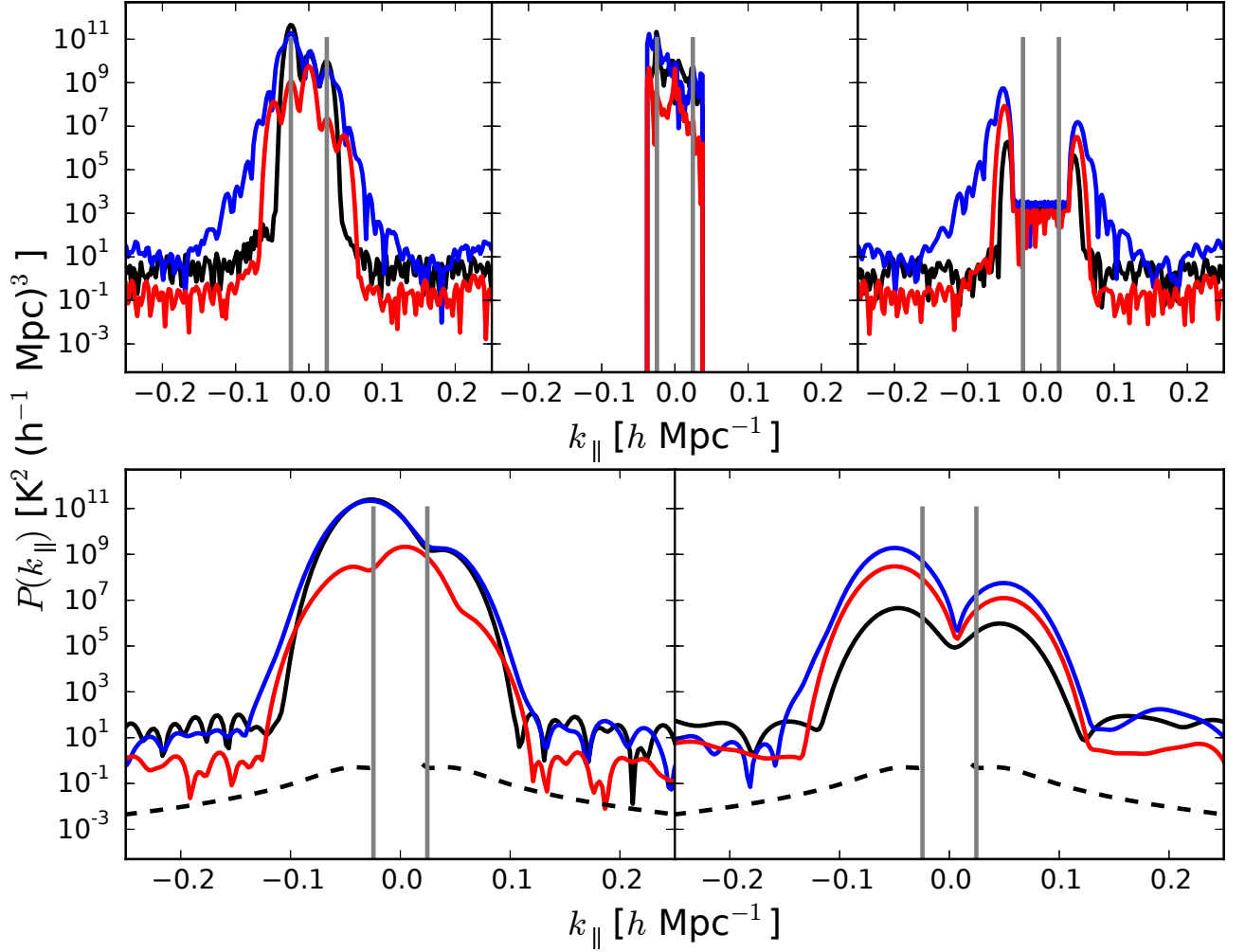


**Figure 3.** Effect of chromaticity of antenna power pattern on foreground delay power spectra.

$k_{\parallel}$ . The two peaks on either side is most severe for the simulated disk pattern followed by that for the *Airy* disk pattern and least for an achromatic power pattern.

We investigate the effect of chromaticity of power pattern in a foreground avoidance strategy that avoids the aforementioned deconvolution of delay spectrum. Application of window functions with high sidelobe suppression have been discussed for mitigating foreground contamination (Thyagarajan et al. 2013). In line with the foreground avoidance strategy, the visibilities from the full band foreground simulation (whose delay power spectrum is shown on the top left) are multiplied by a Blackman-Harris window function of 10 MHz effective bandwidth. The delay power spectra so produced are shown in the panel on the bottom left. Due to the decreased effective bandwidth the resolution of the delay power spectrum appears decreased. Hence, only the  $|k_{\parallel}| \gtrsim 0.14 h \text{ Mpc}^{-1}$  modes remain accessible. Due to the overall lower amplitude of the *Airy* power pattern relative to the simulated dish power pattern and the achromatic pattern, the sidelobe levels of foreground delay power spectra from an *Airy* pattern are lower than the other models by almost two orders of magnitude.

Following a delay-deconvolution based foreground removal strategy, we apply the Blackman-Harris window

of effective bandwidth 10 MHz on the unsubtracted foreground residuals (top right panel) in frequency domain and obtain the delay power spectrum shown in the bottom right panel. It is noted that lesser the chromaticity the more effective the deconvolution process is in lowering the residuals in and around the horizon limits. For instance, the peak of the delay power spectrum using the achromatic beam is lowered by four orders of magnitude relative to the original peak whereas the residuals of delay power spectra with chromatic *Airy* and simulated power patterns is lowered only by two orders of magnitude. However, owing to the ineffective subtraction of the response extending beyond the horizon limits, the sidelobe levels have not been lowered significantly and are within an order of magnitude of each other.

In both strategies, the EoR HI signal power spectrum obtained by simulations with 21cmFAST (Mesinger et al. 2008) is shown for reference (dashed black lines) in the bottom panels.

### 5.3. Constraints on Reflections between Antennas

Patra et al. 2015 (submitted) and Ewall-Wice et al. 2015 (submitted) discuss the measured and simulated reflections between a dish and its feed.

## 6. SUMMARY

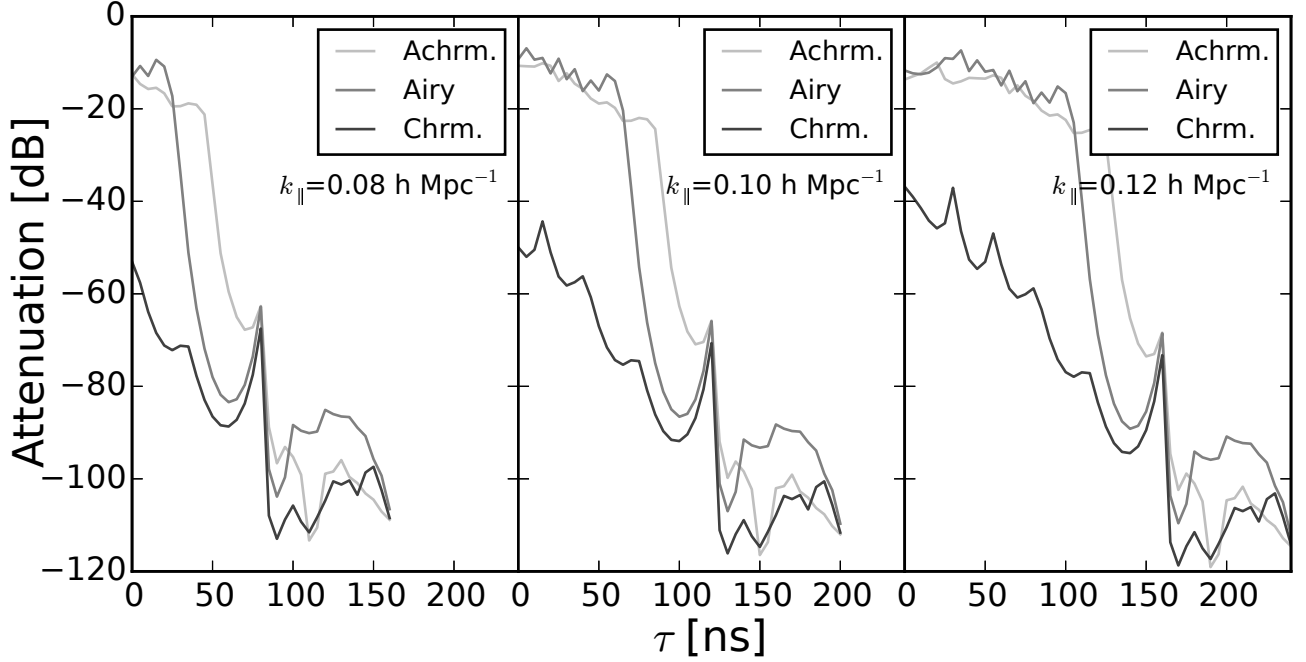


**Figure 4.** Attenuation of foreground power (in dB) from antenna-to-antenna reflections required to keep the reflected foreground power below EoR Hi signal power.

This work was supported by the U. S. National Science Foundation (NSF) through award AST-1109257. DCJ is supported by an NSF Astronomy and Astrophysics Postdoctoral Fellowship under award AST-1401708. JCP is supported by an NSF Astronomy and Astrophysics Fellowship under award AST-1302774.

## REFERENCES

- Ali, S. S., Bharadwaj, S., & Chengalur, J. N. 2008, *MNRAS*, 385, 2166
- Beardsley, A. P., Hazelton, B. J., Morales, M. F., et al. 2013, *MNRAS*, 429, L5
- Bernardi, G., de Bruyn, A. G., Brentjens, M. A., et al. 2009, *A&A*, 500, 965
- Bernardi, G., de Bruyn, A. G., Harker, G., et al. 2010, *A&A*, 522, A67
- Bock, D. C.-J., Large, M. I., & Sadler, E. M. 1999, *AJ*, 117, 1578
- Bowman, J. D., Morales, M. F., & Hewitt, J. N. 2009, *ApJ*, 695, 183
- Bowman, J. D., Cairns, I., Kaplan, D. L., et al. 2013, *PASA*, 30, 31
- Condon, J. J., Cotton, W. D., Greisen, E. W., et al. 1998, *AJ*, 115, 1693
- Datta, A., Bowman, J. D., & Carilli, C. L. 2010, *ApJ*, 724, 526
- de Oliveira-Costa, A., Tegmark, M., Gaensler, B. M., et al. 2008, *MNRAS*, 388, 247
- Di Matteo, T., Perna, R., Abel, T., & Rees, M. J. 2002, *ApJ*, 564, 576
- Dillon, J. S., Liu, A., & Tegmark, M. 2013, *Phys. Rev. D*, 87, 043005
- Dillon, J. S., Liu, A., Williams, C. L., et al. 2014, *Phys. Rev. D*, 89, 023002
- Furlanetto, S. R., & Briggs, F. H. 2004, *New A Rev.*, 48, 1039
- Furlanetto, S. R., Oh, S. P., & Briggs, F. H. 2006, *Phys. Rep.*, 433, 181
- Ghosh, A., Prasad, J., Bharadwaj, S., Ali, S. S., & Chengalur, J. N. 2012, *MNRAS*, 426, 3295
- Gleser, L., Nusser, A., & Benson, A. J. 2008, *MNRAS*, 391, 383
- Iliev, I. T., Shapiro, P. R., Ferrara, A., & Martel, H. 2002, *ApJ*, 572, L123
- Liu, A., Parsons, A. R., & Trott, C. M. 2014a, *Phys. Rev. D*, 90, 023018
- . 2014b, *Phys. Rev. D*, 90, 023019
- Liu, A., & Tegmark, M. 2011, *Phys. Rev. D*, 83, 103006
- Liu, A., Tegmark, M., Bowman, J., Hewitt, J., & Zaldarriaga, M. 2009, *MNRAS*, 398, 401
- Lonsdale, C. J., Cappallo, R. J., Morales, M. F., et al. 2009, *IEEE Proceedings*, 97, 1497
- Madau, P., Meiksin, A., & Rees, M. J. 1997, *ApJ*, 475, 429
- Mauch, T., Murphy, T., Buttery, H. J., et al. 2003, *MNRAS*, 342, 1117
- McQuinn, M., Zahn, O., Zaldarriaga, M., Hernquist, L., & Furlanetto, S. R. 2006, *ApJ*, 653, 815
- Morales, M. F., Bowman, J. D., & Hewitt, J. N. 2006, *ApJ*, 648, 767
- Morales, M. F., Hazelton, B., Sullivan, I., & Beardsley, A. 2012, *ApJ*, 752, 137
- Morales, M. F., & Hewitt, J. 2004, *ApJ*, 615, 7
- Neben, A. R., Bradley, R. F., Hewitt, J. N., et al. 2015, *ArXiv e-prints*, arXiv:1505.07114
- Paciga, G., Albert, J. G., Bandura, K., et al. 2013, *MNRAS*, 433, 639
- Parsons, A. R., & Backer, D. C. 2009, *AJ*, 138, 219
- Parsons, A. R., Pober, J. C., Aguirre, J. E., et al. 2012, *ApJ*, 756, 165
- Parsons, A. R., Backer, D. C., Foster, G. S., et al. 2010, *AJ*, 139, 1468
- Pober, J. C., Parsons, A. R., Aguirre, J. E., et al. 2013, *ApJ*, 768, L36
- Santos, M. G., Cooray, A., & Knox, L. 2005, *ApJ*, 625, 575
- Scott, D., & Rees, M. J. 1990, *MNRAS*, 247, 510
- Sunyaev, R. A., & Zeldovich, Y. B. 1972, *A&A*, 20, 189
- Taylor, G. B., Carilli, C. L., & Perley, R. A., eds. 1999, *Astronomical Society of the Pacific Conference Series*, Vol. 180, *Synthesis Imaging in Radio Astronomy II*
- Thyagarajan, N., Udaya Shankar, N., Subrahmanyam, R., et al. 2013, *ApJ*, 776, 6
- Thyagarajan, N., Jacobs, D. C., Bowman, J. D., et al. 2015a, *ApJ*, 807, L28
- . 2015b, *ApJ*, 804, 14
- Tingay, S. J., Goeke, R., Bowman, J. D., et al. 2013, *PASA*, 30, 7
- Tozzi, P., Madau, P., Meiksin, A., & Rees, M. J. 2000, *ApJ*, 528, 597
- Trott, C. M., Wayth, R. B., & Tingay, S. J. 2012, *ApJ*, 757, 101
- van Haarlem, M. P., Wise, M. W., Gunst, A. W., et al. 2013, *A&A*, 556, A2

Vedantham, H., Udaya Shankar, N., & Subrahmanyam, R. 2012, ApJ, 745, 176

Wang, X., Tegmark, M., Santos, M. G., & Knox, L. 2006, ApJ, 650, 529

Zaldarriaga, M., Furlanetto, S. R., & Hernquist, L. 2004, ApJ, 608, 622